Journal of Materials Chemistry A

Accepted Manuscript

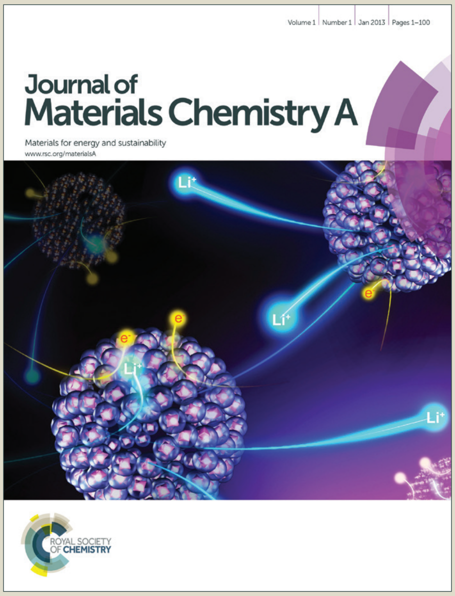

ROYAL SOCIETY OF CHEMISTRY

www.rsc.org/materialsA

Bi_2Te_3@CoNiMo composite as a high performance bifunctional catalyst for the hydrogen and oxygen evolution reactions

*K. Yin [a], Z. D. Cui [a], X. R. Zheng[a, c], X. J. Yang [a, b], S. L. Zhu [a, b], Z. Y. Li [a, b], Y. Q. Liang [a,b] **

[a]*School of Materials Science and Engineering, Tianjin University, Tianjin 300072, China*

[b] *Tianjin Key Laboratory of Composite and Functional Materials, Tianjin 300072, China*

[c] *Key Laboratory of Advanced Ceramics and Machining Technology of the Ministry of Education, Tianjin 300072, China*

---

[*] Corresponding author

E-mail: yqliang@tju.edu.cn (Y.Q. Liang)

Abstract: Hydrogen generated renewably by using solar energy has attracted increasing interest in the renewable energy research community. Hence, efficient electrocatalysts are in demand to reduce costs and energy consumption for the oxygen and hydrogen evolution reaction (OER and HER) activity. Bismuth telluride (Bi_2Te_3)-based materials, as topological insulators (TIs), have been used to explore the fundamental properties of TIs in recent years, but investigation as functional materials for water splitting applications is still quite limited. In this work, electrocatalysts based on Bi_2Te_3 nanosheets have been fabricated, and the HER performance was investigated to further enhance the OER electrocatalytic properties, with certain transition metals (Co, Ni, Mo) selected to provide effective electrocatalytic sites. Therefore, the bifunctional catalyst Bi_2Te_3@CoNiMo was designed for synthesis by a solvothermal and chemical deposition route. The catalyst electrode, Bi_2Te_3@CoNiMo loaded on Ni foam, exhibits higher activity towards both the oxygen and the hydrogen evolution reactions than some traditional metallic catalysts in alkaline electrolyte. The difference in the HER and OER metrics (ΔE = 1.41 V) is comparable to the theoretical value (1.23 V), so that this reaction can be easily driven by a solar cell.

Key words: Bi_2Te_3 nanosheets ; Bi_2Te_3@CoNiMo-Ni foam ; water splitting

Introduction

The conversion of solar energy directly into fuel is a promising solution to the challenges of sustainable energy-conversion and -storage systems, addressing the issues of effective storage and transport. Hydrogen is the cleanest energy source and an ideal energy carrier, so a number of researchers have focused on its production methods. Among the various approaches designed to produce hydrogen, photoelectrochemical water splitting, or water splitting by photovoltaic (PV)–driven electrolysis, has been proven to be a promising method.[1-5] The water splitting reaction consists of two half reactions: the oxygen evolution reaction (OER) and the hydrogen evolution reaction (HER). To conduct electrochemical water splitting, an applied voltage of at least 1.23 V must be applied to provide the thermodynamic driving force. Typically, precious metals or their oxides, such as Pt, RuO_2, and IrO_2, are the most efficient electrocatalysts for the production of molecular hydrogen from water by the HER. Even so, the primary problems in the production of electrolytic hydrogen are the high costs involved and high energy consumption. Hence, to make this technique more efficient and economical, it is imperative to select inexpensive electrode materials that exhibit good hydrogen evolution reaction (HER) activity.

In the past few decades, tremendous efforts have been devoted to developing low-cost and high-efficiency electrocatalysts for water splitting—for example, MoS_2 and NiCu for the H_2 evolution reaction (HER),[6,7] and FeNi, manganese oxide, and mixed-valence transition-metal oxides for the O_2 evolution reaction (OER).[8,9,10] For sustained overall water splitting, the catalysts for the HER and OER must be operated in the same electrolyte.[11] This requirement is a challenge for most of the Earth-abundant catalysts, because a highly active catalyst in acidic electrolyte may not be active in basic electrolyte. Thus, it is crucial to develop a bifunctional catalyst that has high activity towards both the HER and the OER in the same electrolyte (either strongly acidic or strongly basic). Therefore, extensive efforts have been devoted to designing and developing highly efficient and Earth-abundant elements as HER electrocatalysts.

Nickel (Ni) foam is used as the electrode for commercial alkaline electrolysers because of its Earth abundance and porous three-dimensional structure.[12] Recently, Ni foam has received great attention due to its promising activity towards the OER and HER in alkaline electrolyte. Nevertheless, the high overpotential for the cathodic and anodic reactions on Ni foam prevents its large-scale application for water splitting. Hence, efficient electrocatalysts loaded on Ni foam are in demand to reduce the overpotential and increase the efficiency of the OER and HER.

Topological insulators (TIs) are materials with gapped insulating bulks and metallic conducting surfaces.[13,14,15] Bi_2Te_3 has been argued to be a similar three-dimensional (3D) topological insulator with surface quantum-spin-Hall-effect states protected by time-reversal symmetry. The strong spin-orbit coupling in TIs reduces the probability of the electrons being backscattered by surface defects, which lowers the surface resistivity and leads to the formation of topologically protected surface states.[16,17] Recent research has revealed that Bi_2Te_3 is such a strong candidate that it is now referred to as the second generation of TIs that can open up new possibilities for biomedical and optoelectronic applications, such as heat pumps, power generation, solid state refrigeration, cooling for integrated circuit (IC) chips, infrared sensors, optoelectronic sensors, photodetectors, lithium ion batteries, etc.[18-21]

So far, the effects of Bi_2Te_3 on the electrochemical performance of Ni-based anodes have not yet been reported. Herein, an in-situ solvothermal route was used to prepare Bi_2Te_3 nanosheets, and it was found that Ni foam after loading with the Bi_2Te_3 showed a dramatically reduced onset potential of the HER in basic media, but had no promotion effect on the OER. Earth-abundant 3d transition metals (TMs) such as Co, Ni, and Mo have also been demonstrated as particularly promising catalytic materials for the HER and the OER in alkaline electrolytes.[22-26] Therefore, in the present work, CoNiMo alloy nanoparticles (NPs) were deposited on the Bi_2Te_3 nanosheets to obtain a Bi_2Te_3@CoNiMo hybrid, which presents high bifunctional activity towards both the HER and the OER in alkaline electrolyte. Subsequently, the influence of the Co content on the electrocatalytic activity of the CoNiMo alloy NPs with respect to the OER in alkaline solution was also investigated. This work can lead to a new bifunctional catalyst, composed of precious-metal-free catalysts for the HER and OER, which can form the basis for a promising energy storage system that works as a water electrolyser producing H_2 and O_2, which is driven by solar energy.

Experimental

Material preparation

Hexagonal nanosheets of Bi_2Te_3 single crystals were successfully synthesized through a solvothermal method. Typically $BiCl_3$ (1.0 mM), Na_2TeO_3 (1.53 mM), NaOH (15 mM), and different polyvinyl pyrrolidone (PVP) (PVP K40) concentrations (3.13, 9.38, 12.5, 18.75 μM) are added to ethylene glycol (EG, 36 ml) under vigorous magnetic stirring. After 1 h of stirring, the homogeneous solution is transferred into a 60 ml Teflon-lined stainless steel autoclave and heated at 220°C for 36 h. After cooling down to room temperature naturally, the products are filtered and washed with distilled water and ethanol for 3 times each. Finally, the dark products are dried at 60°C.[18] Scanning electron microscope (SEM) images of Bi_2Te_3 nanosheets synthesized by adding different PVP concentrations are shown in Fig. S1 in the Supporting Information.

In order to assemble the CoNiMo NPs, the Bi_2Te_3 nanosheets need to be treated with 25 wt.% NaOH solution at 80°C and slightly washed several times with distilled water to remove the remaining NaOH solution. Then, the preprocessed Bi_2Te_3 nanosheets are mixed with $NiSO_4$ (24.8 mM), Na_2MoO_4 (5.66 mM), different contents of $Co(NO_3)_2$ (3.47, 6.94, 34.7, 69.4 mM), trisodium citrate ($Na_3C_6H_5O_7$, 24.9 mM), and PVP K40 (62.5 uM) in a beaker containing a water/EG solution (1:1 vol%, 50 ml).[27] The mixture is stirred for 1 h, and then, $NaBH_4$ is introduced under stirring. After about 0.5 h, all of the solution is transferred to a water bath kettle under static conditions at 40°C for 1 h, and subsequently rinsed with distilled water and air dried.[28] Energy dispersive spectroscopy (EDS) analyses of the Bi_2Te_3 nanosheets modified with different Co contents are shown in Fig. S2 in Supporting Information. The working electrode is fabricated as follows. Briefly, 0.015 g acetylene black, 0.015 g polyvinyl difluoride, 0.07 g sample and 80 µl N-methyl-2-pyrrolidone were mixed together, and the mixture was directly coated on Ni foam.

Physical characterization

Field emission scanning electron microscopy (FE-SEM, Hitachi S-4800), X-ray diffraction (XRD, RIGAKU/ DMAX), transmission electron microscopy (TEM, Philips Tecnai G2 F20), Raman spectroscopy (DXR, Thermo Electron Corporation), and atomic force microscopy (AFM, Nanoscope III), were employed to characterize the products. Chemical analysis of samples was performed by X-ray photoelectron spectroscopy (XPS) using a PHL1600ESCA instrument equipped with a monochromatic Mg Kα X-ray source (E = 1253.6 eV) source operated at 250 W. Diffuse reflection spectra were collected using a Shimadzu (UV-2700) ultraviolet-visible (UV Vis) spectrophotometer, and the contact angle of the hydrogel was tested on a Theta/Attension Optical Tensiometer.

Electrochemical characterization

The working electrode is the electrodeposited Bi_2Te_3@CoNiMo alloy on Ni foam substrate, with an exposed geometric surface area of 1.2 cm^2. All electrochemical studies were performed using a Gamry Reference 1000 electrochemical workstation in a standard three-electrode set-up. An Ag/AgCl electrode was employed as the reference electrode and Pt foil as the counter electrode. All potentials were referenced to a reversible hydrogen electrode (RHE) by adding a value of ($0.205 + 0.059 \times \text{pH} + E_{\text{Ag/AgCl}}$) V.[29] These measurements were carried out in KOH (0.9 M) at a temperature of 20°C. The electrocatalytic activity of Bi_2Te_3@CoNiMo towards the HER and OER reactions was characterized by linear sweep voltammetry (LSV) at a scan rate of 10 mV s^{-1}, and the scan direction was from positive to negative potential and from negative to positive potential, respectively. The cathodic polarization curves towards the OER were also obtained. The scan rate for polarization measurements was maintained at 10 mV s^{-1}. Electrical impedance spectroscopy (EIS) was conducted under the following conditions: AC voltage amplitude 0 mV, frequency range 10^5–0.01 Hz.

Calculation of the turnover frequency (TOF) was from the following equation:

$$\mathrm{TOF} = \frac{\mathrm{j} \times A}{4 \times m \times F} \qquad (1)$$

Where j is the current density at overpotential, A is the area of the electrode, and m is the number of moles of sample deposited onto the Ni foam. F is the Faraday constant (96500 C mol^{-1}).[10]

Results

The morphology of the Bi_2Te_3 nanosheets is shown in Fig. 1. Fig. 1(a) is typical SEM image of the un-modified Bi_2Te_3 nanosheets. Fig. 1(b) is a low-magnification TEM image of an un-modified Bi_2Te_3 nanosheet. From Fig. 1(a, b), the diameter of the Bi_2Te_3 nanosheets can be estimated to be 400–600 nm. The selected area electron diffraction (SAED) pattern of the synthesized Bi_2Te_3 nanosheet is shown in Fig. 1(c), indicating that the nanosheet is single crystalline. Fig. 1(d) shows a high-resolution TEM image of an un-modified Bi_2Te_3 nanosheet. It clearly shows that the lattice fringes have a spacing of 0.216 nm ~ 0.219 nm), which is in good agreement with the $\{1\bar{2}10\}$ interplanar spacing of Bi_2Te_3. Furthermore, the corresponding EDS mapping analysis for Bi_2Te_3 nanosheet modified by CoNiMo alloy NPs (Fig. 1(f-j)) reveals the homogeneous distribution of Bi and Te, while the other elements, Co, Ni, and Mo, are identified as located in the nanoparticles coated on the Bi_2Te_3 nanosheet. The Ni map shows higher color intensity than the Co and Mo.

XPS is an effective spectroscopic technique to measure the chemical and electronic states of each element in the surface. In order to determine the composition and state of each element in the surface of the modified Bi_2Te_3 nanosheets, XPS spectra of the various regions were collected and are shown with peak deconvolutions in Fig. 2. Fig. 2(a) shows the photoelectron spectrum of Bi 4f. The two peaks at the energy of 157.2 and 162.5 eV, corresponding to the binding energy of Bi $4f_{7/2}$ and Bi $4f_{5/2}$, respectively, are in good agreement with data observed from Bi_2Te_3 single crystal. The two primary peaks at 158.8 and 164 eV are consistent with the Bi 4f spectrum of an oxidized layer of Bi_2Te_3. The photoelectron spectrum of Te 3d is also shown in Fig. 2(b). The scan of the Te 3d region shows peaks at about 572.2 and 582.5 eV, which match the binding energies of Te $3d_{5/2}$ and Te $3d_{3/2}$ of Bi_2Te_3, respectively. The Te 3d scan also shows peaks at about 575.7 and 586.2 eV, which match the binding energies of the Te 3d spectrum of an oxidized layer of Bi_2Te_3.[30] A complex multi-peak structure is observed for the Co 2p spectrum in Fig. 2(c). Three peaks at 781.2, 797.6, and 804.8 eV are observed for Co 2p. These peaks agree well with the values for CoO, Co_3O_4, and Co_2O_3, respectively. A similar complex multi-peak structure is observed in Fig. 2(d). The double peaks located at 856.0 eV and 862.7 eV can be assigned to $2p_{3/2}$ of Ni, and the single peak located at 873.8 eV can be assigned to $2p_{1/2}$ of Ni. These peaks all agree well with the values for NiO. At the same time, a most complex multi-peak structure is observed in Fig. 2(e). The peak at about 229.3 eV is attributed to the binding energy value of Mo $3d_{5/2}$ of MoO_2. The double peak at about 232.1 eV and 233.1 eV is ascribed to the binding energy of Mo $3d_{5/2}$ of MoO_3, and the other double peak at about 235.6 eV and 236.7 eV is consistent with the binding energy value of Mo $3d_{3/2}$ of MoO_3. Fig. 2(f) shows the peaks of O 1s. Two kinds of surface species are observed. The double peak binding energies of 527.5 eV and 530.8 eV can be attributed to the lattice oxygen, while the binding energy of 531.8 eV can be attributed to the adsorbed oxygen. The results of XPS in Fig. 2 prove that the surfaces of the Bi_2Te_3 nanosheets are not only actually oxidized, but also loaded by various oxides of Co, Ni, and Mo.[31,32,33] In order to further analyze the surface oxidation of the doped Bi_2Te_3 nanosheets, we carried out Raman measurements on the different samples with Bi_2Te_3 nanosheets (Fig. S3(a-e) in Supporting Information).

Fig. 3(a) shows an AFM topograph of the Bi_2Te_3 nanosheets. The morphology in this image is obviously that of a nanosheet structure. Fig. 3(b, c) shows scanning gate microscope (SGM) images of the electrical signal within two nanosheets. Fig. 3(d) shows the variation of electrical signal along the green line drawn in Fig. 3(c). It can be observed that the voltage peak was located at the distance of 1970 nm, indicating that the edges of the nanosheets present the highest electrical signal. The additional electron accumulation in the Bi_2Te_3 nanosheets is induced by the conductive probe tip, leading to an increase in current flow. We attribute this effect to a combination of the increase in effective tip-sample contact area near the edges of the nanosheets and the possibility that the TI Bi_2Te_3 is thinner on the sides of the sheets than on top,[34] as well as lower surface resistivity at the edges of the nanosheets.

In order to shed light on the intrinsic advantages of Bi_2Te_3 nanosheets on Ni foam, the catalytic kinetics of this sample with respect to the HER was examined by LSV scanned from different initial potentials (Fig. 4(a)) to investigate the origin of the synergistic effect. The inset in Fig. 4(a) shows cyclic voltammograms (CV) for the Ni foam before and after it is loaded by Bi_2Te_3 nanosheets. There is no redox peak for the pure Ni foam in the CV results, but two anodic peaks located at +0.90 V and +1.45 V appear in the Ni foam after loading with the Bi_2Te_3 nanosheets, which can be attributed to the oxidation of the Bi_2Te_3 nanosheets: $Te^{-2} \rightarrow Te^{0}$ and $Te^{0} \rightarrow Te^{+4}$, respectively. Accordingly, the cathodic peaks at 0.23 V and -0.29 V are assigned to the reduction of $Te^{+4} \rightarrow Te^{0}$ and $Te^{0} \rightarrow Te^{-2}$, respectively. Fig. 4(a) shows LSV curves for different initial voltages of doped Bi_2Te_3 nanosheets on Ni foam in 0.9 M KOH solution. It can be seen from Fig. 4(a) that, with the initial voltage decreases, the peak for the reduction of the Te^{0} is shifted to higher potential, while the peak intensity is also reduced. The reduction peak from Te^{0} to Te^{-2} cannot be detected, since the potential cut-off was held below 0.3 V.[35,36] The high intensity of the reduction peaks suggest that a direct reaction is the predominant reaction on Bi_2Te_3. Fig. 4(b) shows the HER characteristics of different catalyst electrodes. The current density required to begin to generate H_2 bubbles is an important performance index of an HER catalyst. We have marked the potential where H_2 bubbles begin to be generated as the initial potential. Several remarks on the results are required. First, the HER activity for Bi_2Te_3-Ni foam and CoNiMo-Ni foam are relatively lower, because the monocomponent catalyst with either Bi_2Te_3 or CoNiMo alloy has a negligible effect towards improving the HER performance of Ni foam. Second, for the HER catalyst obtained by using Bi_2Te_3@$Co_{69.4}$NiMo-Ni foam, the lowest voltage among the samples was required to generate H_2, and this confirms that the synergetic effects arising from the interactions between the CoNiMo catalyst and the Bi_2Te_3 substrate could improve the electrocatalytic performance. Third, the reduction peak is visible on the LSV curves before H_2 evolution for the sample of Bi_2Te_3-Ni foam, but this peak can be eliminated by modification with CoNiMo NPs. Hence, the onset potential of H_2 evolution decreases dramatically, highlighting the much enhanced HER activity of the Bi_2Te_3@CoNiMo-Ni foam due to the improved charge transport by introducing the CoNiMo NPs, and this potential value is much lower than those of the reported Earth-abundant HER catalysts in alkaline media.[37,38] Finally, the initial potential difference between the Bi_2Te_3@CoNiMo-Ni foam and the other four samples, Ni foam, Bi_2Te_3-Ni foam, CoNiMo-Ni foam, and Pt/C-Ni foam, are 0.23, 0.18, 0.38, and -0.04 V, respectively. The smallest difference of -0.04V indicates that the HER activity of Bi_2Te_3@CoNiMo-Ni foam (with initial potential of -0.1 V) is almost comparable to that of the highly active Pt/C HER catalyst (with initial potential of -0.06 V). In addition, when the Bi_2Te_3@CoNiMo-Ni foam begins to generate H_2 bubbles, the corresponding current density reaches as high as 60 mA cm^{-2}, which is 60 mA cm^{-2} higher than for Ni foam and even 18 mA cm^{-2} higher than for the Pt/C-Ni foam, suggesting its favorable reaction kinetics. Furthermore, catalytic activity expressed in TON (moles of H_2 per moles catalyst) is an important descriptor of HER activity. The calculated TON also indicate the high HER performance of Bi_2Te_3@CoNiMo-Ni foam. (Fig. S4, Supporting Information).

Fig. 5 shows the OER activity of the Ni foam, Bi_2Te_3-Ni foam, Bi_2Te_3@CoNiMo-Ni foam, and RuO_2-Ni foam samples. A slow scan rate (10 mV s^{-1}) was applied during the OER test to minimize the capacitive current. Fig. 5(b) summarizes the onset potentials (E_{onset}) and potentials required to reach J= 10 mA cm^{-2} ($E_{J=10\text{ mA cm}^{-2}}$) of the OER catalyzed by the prepared catalysts according to Fig. 5(a). Several features are worth noting. The Ni foam exhibits negligible catalytic activity, as shown in the polarization curve recorded in 0.9 M KOH solution (Fig. 5(a)), and the Bi_2Te_3-Ni foam also displays a low OER response with a high onset potential at ~1.66 V vs.

reversible hydrogen electrode (RHE), while the Bi_2Te_3@CoNiMo-Ni foam shows the lowest onset potential (~1.26 V) for the OER current among these four catalysts, indicating that the synergistic effects between Bi_2Te_3 and CoNiMo can significantly improve the catalytic activity. Remarkably, the OER current of Bi_2Te_3@CoNiMo-Ni foam greatly exceeds that of RuO_2-Ni foam (coated on Ni foam with the same loading amount) and it can produce a 18.6% power saving compared to the RuO_2-Ni foam by using the equation of "P = IxV" to calculate the power. Similarly, the Bi_2Te_3@CoNiMo-Ni foam needs much lower overpotential to reach 10 mA cm^{-2}, a reference value in evaluating OER catalysts, especially for a solar water splitting device that works with 10% efficiency.[39] The Bi_2Te_3@CoNiMo-Ni foam affords a current density of 10.0 mA cm^{-2} at 1.31 V (Fig. 5(b)), lower than that of RuO_2-Ni foam at 1.61 V, Bi_2Te_3-Ni foam at 1.73 V, and Ni foam at 1.78 V.

To gain further insight into the OER activities of these catalysts, Tafel plots, a valuable type of measurement to study the kinetics of the OER, were retrieved from the anodic sweep and are presented in Fig. 5(c). A linear dependency of E vs. log(J) was achieved for all the samples, and this is displayed with different slopes and intercepts. The overall Tafel slopes follow the order of Bi_2Te_3@CoNiMo-Ni foam (38.54 mV dec^{-1}) < RuO_2-Ni foam (50.08) < Bi_2Te_3-Ni foam (81.39) < Ni foam (116.0). The Bi_2Te_3@CoNiMo-Ni foam displays the lowest Tafel slope, which is in agreement with the results of LSV. Moreover, on the basis of the assumption that all of the active metal atoms in the catalysts drop-casted on the glassy carbon electrode are catalytically active towards the OER,[40,41] Fig. 5(d) shows the calculated OER turnover frequencies (TOFs) at different overpotentials. It is observed that the TOF of the Bi_2Te_3@CoNiMo-Ni foam is higher than that of the other catalysts under the same applied potentials, while the TOF values for the Ni foam are almost negligible. It is worth noting that the TOF values of the Bi_2Te_3@CoNiMo-Ni foam and the Bi_2Te_3-Ni foam at an overpotential of 0.27 V is about 0.213 $s^{-1}$and 0.134 s^{-1}, which are almost 6 and 2 times higher than for the RuO_2-Ni foam catalyst, respectively. Moreover, the TOF value of Bi_2Te_3@CoNiMo-Ni foam is roughly 10-fold higher than that of the reported IrO_x (0.0089 s^{-1}) catalyst, suggesting high OER activity on Bi_2Te_3@CoNiMo.[42]

In order to reveal the effects of the Co content on the OER activity of Bi_2Te_3@CoNiMo-Ni foam catalysts, the linear sweep voltammetry (LSV) curves of OERs for Bi_2Te_3@CoNiMo-Ni foam catalysts with different Co concentrations are shown in Fig. 6(a). For the Bi_2Te_3@CoNiMo-Ni foam catalysts, the onset potential of the OER was negatively shifted with increasing Co composition, while the potential required to reach J = 10 mA cm^{-2} ($E_{J=10\ mA\ cm^{-2}}$) also decreased simultaneously. Fig. 6(a) demonstrates that the OER activity of the Bi_2Te_3@CoNiMo-Ni foam catalysts is monotonically enhanced with increasing Co content from

3.47 mM to 69.4 mM. The Bi_2Te_3@$Co_{69.4}$NiMo-Ni foam with the optimal Co content exhibited the highest OER activity, with 1.31 V overpotential at 10 mA cm^{-2} in 0.9 M KOH, compared to 1.61 V overpotential observed on the noble oxide RuO_2 catalyst. The significant enhancement of the OER activity indicates that the Co is involved in active sites on the catalyst surface. This result may be due to the different catalyst morphology and valence state of the element resulting from the synthesis method and electrode preparation technique.[38,43-47] This will be discussed later in detail.

The information obtained from the Tafel plots can be used to determine the mechanisms behind an electrochemical process and also to compare the electrocatalytic activity of various electrocatalysts. The Tafel slope depends not only on the reaction mechanism and the material's intrinsic activity toward the process, but also on its three-dimensional structure, porosity, and possession of grains with unique surface arrangements of atoms and electrocatalytic activities.[48]

In the case of multicomponent electrodes, the presence of more than one linear region might be attributed to a given reaction possessing two different mechanistic pathways, provided that other phenomena do not give rise to a different Tafel slope. At high overpotential values, the process is under mass-transport control, while the OER process is controlled by the speed of surface reactions in the low overpotential regions. The Tafel plots for the Bi_2Te_3@CoNiMo-Ni foam electrodes with different Co content display similar features over the entire overpotential range. In the lower activation overpotential (η) linear region, the Tafel slopes are low, and they increase in the order of Bi_2Te_3@$Co_{69.4}$NiMo-Ni foam (43.26mV dec^{-1}) < Bi_2Te_3@$Co_{34.7}$NiMo-Ni foam (61.20)< Bi_2Te_3@$Co_{6.94}$NiMo-Ni foam (78.66) < Bi_2Te_3@$Co_{3.47}$NiMo-Ni foam (81.71). The reason can be attributed to the greater electron transfer induced by the oxidation of Co, which determines the OER rate dominated by surface reactions. On the other hand, there is a high η linear region where the slopes are high. The Tafel slope of Bi_2Te_3@$Co_{69.4}$NiMo-Ni foam is 224.8 mV dec^{-1}, which is similar to those for the Bi_2Te_3@$Co_{34.7}$NiMo-Ni foam (220.3 mV dec^{-1}) and the Bi_2Te_3@$Co_{6.94}$NiMo-Ni foam (218.8 mV dec^{-1}), but significantly lower than the value of the Bi_2Te_3@$Co_{3.47}$NiMo-Ni foam (406.9 mV dec^{-1}). The lower Tafel slope value of Bi_2Te_3@$Co_{69.4}$NiMo-Ni foam is ascribed to more facile mass transfer inside the large particles (see Fig. S2(d) in Supporting Information). On the contrary, the highest Tafel slope value of Bi_2Te_3@$Co_{3.47}$NiMo-Ni foam indicates the highest transfer resistance, which is further proved by the EIS results. Ionic and charge transport are crucial factors for the performance of these efficient electrochemical OER catalysts, due to the mediating role that the Co oxides play in the OER, as discussed above. Thus, electrochemical impedance spectroscopy (EIS) measurements were employed under OER reaction conditions (Fig. 6(c)), with the aim of discovering direct evidence for the remarkable OER activities controlled by the Co oxide activity relations. The charge transfer resistance for each sample, corresponding to the semicircular diameter in the EIS spectrum, was obtained from the fitted equivalent circuit (inset in Fig. 6(c)), where R_s represents the resistance of the electrolyte, R_f is the resistance of the catalyst layer, and C_f the capacitance. C_{dl} is the double layer capacitance, and R_{ct} the charge transfer resistance. All the parameters obtained from this equivalent circuit are listed in Table S1 in the Supporting Information. The uncompensated solution resistance (R_s, ohmic resistance) in the high frequency region is comparable for all catalysts.[49] R_f follows the order Bi_2Te_3@$Co_{69.4}$NiMo-Ni foam (0.386 Ω) < Bi_2Te_3@$Co_{34.7}$NiMo-Ni foam (0.7664 Ω)< Bi_2Te_3@$Co_{6.94}$NiMo-Ni foam (1.431 Ω) < Bi_2Te_3@$Co_{3.47}$NiMo-Ni foam (2.634 Ω), in perfect correlation with the OER (Fig. 6(a)) activity trend, implying an inverse relationship. These results suggest that the conductivity of the Bi_2Te_3@$Co_{69.4}$NiMo-Ni foam increases with the Co content, which indicates a much faster electron transfer process during electrochemical reactions.

The turnover frequencies (TOFs) of the Bi_2Te_3@CoNiMo-Ni foam catalysts at different overpotentials were calculated in 0.9 M KOH, assuming that all of the metal ions in the catalysts were involved in the electrochemical reaction. The TOF values of all catalysts showed a clear increase with overpotential. In addition, the overall TOF value at different overpotentials increases with the Co content for the four samples (see Fig. 6(d)). It should be noted that the Co content and the morphology of the CoNiMo alloy NPs could affect the OER performance of the catalyst, since CoO and Co_3O_4 serve as active sites, as well as because its facile mass transfer dominates the OER rate.

Moreover, this excellent OER activity of the Bi_2Te_3@CoNiMo-Ni foam is not only better than those of most of the state-of-the-art Co/Mo/Ni-based transition-metal electrocatalysts[46,50-53] and of non-metal catalysts, but also superior to those of other catalysts supported by Ni foam, such as Ni-substituted Co_3O_4 nanowire arrays grown on Ni foam (1.60 V, pH 14).[54,55,56] A detailed comparison of different highly active OER catalysts with various electrode configurations is shown in Table S2 in the Supporting Information, further confirming the outstanding catalytic behavior of Bi_2Te_3@CoNiMo-Ni foam.

Discussion

Fig. 7 shows a linear sweep voltammogram (LSV) for the optimum sample of modified-Bi_2Te_3 nanosheets on Nickel (Ni) foam in 0.9 M KOH solution. Ni foam is used as the electrode for commercial alkaline electrolysers because of its Earth-abundance and porous three-dimensional structure. The high performances of the CoNiMo modified-Bi_2Te_3 nanosheets towards both the OER and the HER in strongly alkaline solutions make it an exceptional bifunctional catalyst. For the HER, the hydrogen evolution starts at -60 mA cm^{-2} when the electrode begins to bubble, which corresponds to the initial potential of -0.1 V. For the OER, the oxygen evolution starts at the potential of 1.31 V (current density of 10 mA cm^{-2}). The relative electric potential difference is 1.41 V ($\triangle E$ = 1.41 V). A schematic illustration of the electrochemical reactions is presented in the inset. For the two-electrode water splitting measurement, the same catalyst electrode is used for both the HER and OER, and the reactions are driven by solar energy (Video S1 and Fig. S5, Supporting Information). When the electrode is used for the HER, the response of the surface of the foam is commonly expressed as:

$2H^+ + 2e^- = H_2$ (2)

When it is used for the OER, the response of the surface is always expressed as:

$4OH^- - 4e^- = 2H_2O + O_2$ (3)

Bi_2Te_3 has been argued to be a 3D topological insulator (TI) with surface quantum-spin-Hall-effect states protected by time-reversal symmetry. The strong spin-orbit coupling in TIs reduces the probability of the electrons being backscattered by surface defects, which lowers the surface resistivity and leads to the formation of topologically protected surface states.[57,58] Meanwhile, based on previous results,[18] Bi_2Te_3 has a tetradymite crystal structure (as shown in Fig. S6 in Supporting Information): along the *c*-axis, ionic and covalent bonds join the five hexagonal closed-packed layers (denoted as the quintuple layer (QL) [Te1-Bi-Te2-Bi-Te1]), with van der Waals force connecting two sets of quintuple layers, which is the fundamental building block in the Bi_2Te_3 crystal cell. The structure of Bi_2Te_3 is similar to that of graphene, enhancing its electronic transmission capability, which is of benefit for the HER and OER.

Several reasons should be noted for the excellent HER performance of Bi_2Te_3@CoNiMo-Ni foam catalyst. First, the Bi_2Te_3 nanosheets are weak hydrophilic, with contact angles of 69° , while after modification with CoNiMo NPs, the wettability becomes more hydrophilic (Fig. S7 in Supporting Information), which leads to the sharp increase of HER activity. Second, Bi_2Te_3-Ni foam can increase the current density over that of Ni foam due to the reduction reaction of the Te^0/Te^{-2} transition, but it can’t improve its overpotential in the HER. Bi_2Te_3 modified by CoNiMo NPs can eliminate the redox reaction of Bi_2Te_3 and further improve the overpotential of Ni foam. It is the synergistic effects between Bi_2Te_3 and the CoNiMo NPs that contribute to the promotion of current density. Finally, the topological surface states of topological insulators (TIs) possess a single spin-polarized Dirac cone originated from strong spin-orbit coupling.[59-61] In the vicinity of the K-points the energy depends linearly on the wave vector. Electrons propagating through Bi2Te3 lattice effectively lose their mass, producing quasi-particles with higher mobility. It means that the bulk Bi2Te3 was insulating, but the local surface regions show conductive states. This will accelerates the electronic transmission and lead to high performance of the Bi_2Te_3@CoNiMo composite. The enhanced performance of Bi_2Te_3@CoNiMo-Ni foam catalyst is also related to the decrease in the band gap as well as lower surface resistivity at the edges of the nanosheets. (Fig. 3 and S8 in Supporting Information), with the electron transfer from the CoNiMo to the Bi_2Te_3 conduction or valence band giving rise to the fast charge transition in electro-induced water splitting reactions.

The remarkable composite structure composed of strongly coupled Bi_2Te_3 and CoNiMo NPs reveals its great potential for the electrocatalytic OER. The outstanding OER activity of Bi_2Te_3@$Co_{69.4}$NiMo-Ni foam catalyst originates from its high Co content (high concentration of active sites), reduced grain boundaries in CoNiMo NPs (fast mass transport), and strong coupling between the Bi_2Te_3 and the CoNiMo (good electron conductivity). Firstly, Bi_2Te_3 features a high Co content of 69.4 mM, ,which surpasses the values reported for the typical catalysts,[62,63] because a high Co content is apt to lead to the formation of CoO and Co_3O_4 (Fig. S3 in Supporting Information), both of which exhibit higher OER activity.[64] Due to the complex amorphous structure of CoNiMo catalyst, however, the mechanisms of OER activity vary with the Co content and still need to be further investigated. Secondly, to illustrate the importance of the reduction in grain boundaries in CoNiMo NPs, the Tafel slopes in the high potential region for the Bi_2Te_3@CoNiMo-Ni foam catalysts with different Co content reveal that a smaller size of the CoNiMo NPs restricts mass transfer in the catalyst due to the increase in grain boundaries. These facts demonstrate that the larger size of the CoNiMo NPs formed with higher Co content favors the easy infiltration of electrolyte, the efficient transfer of reactants (that is, OH^- ions), and the fast emission of products (that is, O_2). Thirdly, the poor electron transfer in amorphous CoNiMo NPs is the primary barrier limiting their use in electrocatalytic applications,[65] which is conquered herein by the strong coupling with Bi_2Te_3 with highly conductive sheet edges (as evidenced by AFM). The smooth transfer of the generated catalytic current between the Bi_2Te_3 and the CoNiMo NPs is proven by the UV-visible spectra (Fig. S8 in Supporting Information), and their band gap is reduced effectively compared with mono-component Bi_2Te_3.

Moreover, the short-term stability of the Bi_2Te_3 and Bi_2Te_3@CoNiMo-Ni foam catalysts with different Co content was investigated by chronoamperometry. It was observed that no obvious current degradation appears in Bi_2Te_3, implying that the Bi_2Te_3 catalyst was not deactivated in the KOH medium. Furthermore, it is exciting to observe that after a 1 h test, the current density showed no apparent change in the series of Bi_2Te_3@CoNiMo-Ni foam catalysts, except for the slight drop in the beginning (Fig. S9 in Supporting Information). This activity decrease may be caused by a small mass loss of the catalyst due to its partial peeling by rapid oxygen generation, which is also confirmed by the in-situ Fourier transform infrared (FT-IR) results (Fig. S10 in Supporting Information)

Conclusions

We have successfully synthesized Bi_2Te_3-supported CoNiMo NPs as a catalyst for the HER and OER through solvothermal and chemical deposition routes. TEM characterization showed that all CoNiMo catalysts are predominantly amorphous, containing a small amount of metal oxide. These catalysts exhibited remarkable catalytic performances towards the HER and OER in alkaline electrolytes. For the HER, the Bi_2Te_3@CoNiMo-Ni foam catalyst showed an onset overpotential of only 0.1 V vs. RHE, which is comparable to that of Pt/C. The enhanced HER activity exists because the wettability of Bi_2Te_3@CoNiMo is changed to hydrophilic, and because the modification with CoNiMo NPs can eliminate the redox reaction of Bi_2Te_3 and further improve the overpotential of Ni foam. The Co concentration could be modulated during the preparation of the catalysts. These catalysts exhibited increasing catalytic performance towards the OER with increasing Co concentration. The optimized Bi_2Te_3@$Co_{69.4}$NiMo-Ni foam exhibits the lowest onset overpotential, a significantly smaller deviation of the polarization curve in the lower potential region, and higher electrode film stability. The Bi_2Te_3@$Co_{69.4}$NiMo-Ni foam exhibited overpotential of 0.08 V at 10 mA cm^{-2}, which is amongst the smallest overpotentials among the non-precious-metal OER catalysts in an alkaline electrolyte reported so far. The results demonstrate that the introduction of metal (CoNiMo) into the Bi_2Te_3 catalysts can synergistically enhance the HER and OER activity. We believe that this new catalyst will be a promising bifunctional catalyst with superior activity and high long-term stability for water splitting driven by solar energy.

Acknowledgment

Financial support by National Natural Science Foundation of China (51402211) and Natural Science Foundation of Tianjin (15JCQNJC03600) are gratefully acknowledged.

References:

[1] J. S. Luo, J. H. Im, M. T. Mayer, M. Schreier, M. K. Nazeeruddin, N. G. Park, S. D. Tilley, H. J. Fan and M. Graetzel, *Science*, 2014, **345**, 1593-1596.
[2] M. W. Kanan and D. G. Nocera, *Science*, 2008, **321**, 1072–1075.
[3] S. Y. Reece, J. A. Hamel and K. Sung, *Science*, 2011, **334**, 645–648.
[4] J. Brillet, J. H. Yum, M. Cornuz, T. Hisatomi, R. Augustynski, J. Augustynski, M. Graetzel and K. Sivula, *Nat. Photonics*, 2012, **6**, 824–828.
[5] J. S. Luo, S. K. Karuturi, L. Liu, L. T. Su, A. I. Y. Tok and H. J. Fan, *Sci. Rep.*, 2012, **2**, 451.

[6] B. B. Li, S. Z. Qiao, X. R. Zheng, X. J. Yang, Z. D. Cui, S. L. Zhu, Z. Y. Li and Y. Q. Liang, *J. Power Sources*, 2015, **284**, 68-76.

[7] Z. W. Yin and F.Y. Chen, *J. Power Sources*, 2014, **265**, 273-281.

[8] A. Ramirez, P. Hillebrand, D. Stellmach, M. M. May, P. Bogdanoff and S. Fiechter, *J. Phys. Chem. C*, 2014, **118**, 14073−14081.

[9] X. M. Ge, Y. Y. Liu, F. W. T. Goh, T. S. A. Hor, Y. Zong, P. Xiao, Z. Zhang, S. H. Lim, B. Li and X. Wang, *ACS Appl. Mater. Interfaces*, 2014, **6**, 12684−12691.

[10] X. Long, J. K. Li, S. Xiao, K. Y. Yan, Z. L. Wang, H. N. Chen and S. H. Yang, *Angew. Chem.*, *Int. Ed.*, 2013, **53**, 7584 –7588.

[11] E. A. Hernandez-Pagan, N. M. Vargas-Barbosa, T. H. Wang, Y. X. Zhao, E. S. Smotkin and T. E. Mallouk, *Energy Environ. Sci.*, 2012, **5**, 7582–7589.

[12] K. Zeng, and D. Zhang, *Prog. Energy Combust. Sci.*, 2010, **36**, 307–326.

[13] L. Fu and C. L. Kane, *Phys. Rev. B*, 2007, **76**, 045302.

[14] D. Hsieh, Y. Xia, L. Wray, D. Qian, A. Pal, J. H. Dil, J. Osterwalder, F. Meier, G. Bihlmayer and C. L. Kane, *Science*, 2009, **323**, 919-922.

[15] Z. Alpichshev, J. G. Analytis, J. H. Chu, I. R. Fisher, Y. L. Chen, Z. X. Shen, A. Fang and A. Kapitulnik, *Phys. Rev. Lett.*, 2010, **104**, 016401.

[16] J. J. Cha and Y. Cui, *Nature Nanotechnology*, 2012, **7**, 85–86.

[17] D. Hsieh, Y. Xia, D. Qian, L. Wray, J. H. Dil, F. Meier, J. Osterwalder, L. Patthey, J. G. Checkelsky and N. P. Ong, *Nature*, 2009, **460**, 1101–1105.

[18] B. Liu, W. Y. Xie, H. Li, Y. R. Wang, D. P. Cai, D. D. Wang, L. L. Wang, Y. Liu, Q. H. Li and T. H. Wang, *Sci. Rep.*, 2014, **4**, 4639.

[19] B. C. Sales, *Science*, 2002, **295**, 1248-1249.

[20] R. Venkatasubramanian, E. Siivola, T. Colpitts and B. O'Quinn, *Nature*, 2001, **413**, 597-602.

[21] F. F. Tu, J. Xie, G. S. Cao and X. B. Zhao, *Materials*, 2012, **5**, 1275-1284.

[22] J. Deng, P. J. Ren, D. H. Deng, L. Yu, F. Yang and X. H. Bao, *Energy Environ. Sci.*, 2014, **7**, 1919–1923.

[23] A. Doner, I. Karci and G. Kardas, *Int. J. Hydrogen Energy*, 2012, **37**, 9470–9476.

[24] A. Doner, R. Solmaz and G. Kardas, *Int. J. Hydrogen Energy*, 2011, **36**, 7391–7397.

[25] V. V. Kuznetsov, A. A. Kalinkina, T. V. Pshenichkina and V. V. Balabaev, *Russ. J. Electrochem.*, 2008, **44**, 1350–1358.

[26] M. Torabi and S. K. Sadrnezhaad, *Curr. Appl. Phys.*, 2010, **10**, 72–76.

[27] W. C. Sheng, A. P. Bivens, M. Myint, Z. B. Zhuang, R. V. Forest, Q. R. Fang, J. G. Chen and Y. S. Yan, *Energy Environ. Sci.*, 2014, **7**, 1719–1724.

[28] Y. Q. Liang, Z. D. Cui, S. L. Zhu, Y. Liu and X. J. Yang, *J. Catal.*, 2011, **78**, 276–287.

[29] T. Y. Ma, S. Dai, M. Jaroniec and S. Z. Qiao, *J. Am. Chem. Soc.*, 2014, **136**, 13925−13931.

[30] J. P. Fu, S. Y. Song, X. G. Zhang, F. Cao, L. Zhou, X. Y. Li and H. J. Zhang, *Cryst. Eng. Comm.*, 2014, **14**, 2159–2165.

[31] L. Silipigni, F. Barreca, E. Fazio, F. Neri, T. Spano, S. Piazza, C. Sunseri and R. Inguanta, *J. Phys. Chem. C*, 2014, **118**, 22299−22308.

[32] N. Kitakatsu, V. Maurice, C. Hinnen and P. Marcus, *Surf. Sci.*, 1998, **407**, 36-58.

[33] N. Q. Wu, L. Fu, M. Su, M. Aslam, K. C. Wong and V. P. Dravid, *Nano Lett.*, 2004, **4**, 383-386.

[34] X. Zhou, S. A. Dayeh, D. Wang and E. T. Yu, *Appl. Phys. Lett.*, 2007, **90**, 233118.

[35] J. Y. He, S. L. Mao, S. Y. Zhang, H. L. Niu, B. K. Jin and Y. P. Tian, *Mater. Sci. Semicond. Process.*, 2009, **12,** 217–223.

[36] G. R. Li, C. Z. Yao, X. H. Lu, F. L. Zheng, Z. P. Feng, X. L. Yu, C. Y. Su and Y. X. Tong, *Chem. Mater.*, 2008, **20,** 3306–3314.

[37] A, Safavi, S. H. Kazemi and H. Kazemi, *Fuel*, 2014, **118**, 156-162.

[38] M. Xia, T. Lei, N. L. Lv and N. F. Li, *Int. J. Hydrogen Energy*, 2014, **39**, 4794-4802.

[39] Y. Gorlin and T. F. Jaramillo, *J. Am. Chem. Soc.*, 2010, **132**, 13612−13614.

[40] M. Gong, Y. G. Li, H. L. Wang, Y. Y. Liang, J. Z. Wu, J. G. Zhou, J. Wang, T. Regier, F. Wei and H. J. Dai, *J. Am. Chem. Soc.*, 2013, **135**, 8452 – 8455.

[41] X. Zou, A. Goswami and T. Asefa, *J. Am. Chem. Soc.*, 2013, **135**, 17242 – 17245.

[42] L. Trotochaud, J. K. Ranney, K. N. Williams and S. W. Boettcher, *J. Am. Chem. Soc.*, 2012, **134**, 17253−17261.

[43] N. H. Chou, P. N. Ross, A. T. Bell and T. D. Tilley, *ChemSus.Chem*, 2011, **4**, 1566−1569.

[44] A. J. Esswein, M. J. McMurdo, P. N. Ross, A. T. Bell and T. D. Tilley, *J. Phys. Chem. C*, 2009, **113**, 15068−15072.

[45] K. L. Pickrahn, S. W. Park, Y. Gorlin, H. B. R. Lee, T. F. Jaramillo and S. F. Bent, *Adv. Energy Mater.*, 2012, **2**, 1269−1277.

[46] Y. Y. Liang, Y. G. Li, H. L. Wang, J. G. Zhou, J. Wang, T. Regier and H. J. Dai, *Nat. Mater.*, 2011, **10**, 780−786.

[47] Y. Liu, D. C. Higgins, J. Wu, M. Fowler and Z. Chen, *Electrochem. Commun.*, 2013, **34**, 125−129.

[48] J. van Drunen, B. K. Pilapil, Y. Makonnen, D. Beauchemin, B. D. Gates and G. Jerkiewicz, *ACS Appl. Mater. Interfaces*, 2014, **6**, 12046−12061.

[49] Z. He and F. Mansfeld, *Energy Environ. Sci.*, 2009, **2**, 215−219.

[50] W. J. Zhou, X. J. Wu, X. H. Cao, X. Huang, C. L. Tan, J. Tian, H. Liu, J. Y. Wang and H. Zhang, *Energy Environ. Sci.*, 2013, **6**, 2921-2924.

[51] S. Chen, J. Duan, M. Jaroniec and S. Z. Qiao, *Angew. Chem., Int. Ed.*, 2013, **52**, 13567-13570.

[52] S. Mao, Z. Wen, T. Huang, Y. Hou and J. Chen, *Energy Environ. Sci.*, 2014, **7**, 609-616.

[53] X. X. Zou, J. Su, R. Silva, A. Goswami, B. R. Sathe and T. Asefa, *Chem. Commun.*, 2013, **49**, 7522-7524.

[54] H. Y. Jin, J. Wang, D. F. Su, Z. Z. Wei, Z. F. Pang and Y. Wang, *J. Am. Chem. Soc.*, 2015, **137**, 2688−2694.

[55] S. Q. Chen, Y. F. Zhao, B. Sun, Z. M. Ao, X. Q. Xie, Y. Y. Wei and G. X. Wang, *ACS Appl. Mater. Interfaces*, 2015, **7**, 3306−3313.

[56] Y. H. Wang, G. X. Zhang, W. W. Xu, P. B. Wan, Z. Y. Lu, Y. P. Li, X. M. Sun, *ChemElectroChem*, 2014, **1**, 1138 – 1144.

[57] J. J. Cha and Y. Cui, *Nature Nanotechnology*, 2012, **7**, 85-86.

[58] D. Hsieh, L. Wray, J. H. Dil, F. Meier, J. Osterwalder, L. Patthey, J. G. Checkelsky and N. P. Ong, *Nature*, 2009, **460**, 1101-U59.

[59] X. L. Qi and S. C. Zhang, *Phys. Today*, 2010, **63**, 33–38.

[60] J. E. Moore, *Nature*, 2010, **464**, 194–198.

[61] M. Z. Hasan and C. L. Kane, *Rev. Mod. Phys.*, 2010, **82**, 3045–3067.

[62] M. R. Gao, Y. F. Xu, J. Jiang, Y. R. Zheng and S. H. Yu, *J. Am. Chem. Soc.*, 2012, **134,**

2930-2933.

[63] Y. R. Zheng, M. R. Gao, Q. Gao, H. H. Li, J. Xu, Z. Y. Wu and S. H. Yu, *Small*, 2015, **11,** 182-188.

[64] X. J. Liu, Z. Chang, L. Luo, T. H. Xu, X. D. Lei, J. F. Liu and X. M. Sun, *Chem. Mater.*, 2014, **26,** 1889-1895.

[65] M. Plata-Torres, A. M. Torres-Huerta, M. A. Dominguez-Crespo, E. M. Arce-Estrada, C. Ramirez-Rodriguez, *Int. J. Hydrogen Energy*, 2007**, 32,** 4142 – 4152.

Author contribution statement

K. Yin and Y. Q. Liang wrote the main manuscript text, and K. Yin finished all the experiments. Z. D. Cui prepared Figs. 1 and 2. X. R. Zheng prepared Fig. 3. X. J. Yang and S. L. Zhu prepared the Supporting Information. Z. Y. Li recorded the supporting video. All authors reviewed the manuscript.

Figure Captions

Figure 1 | (a) SEM image of unmodified Bi_2Te_3 nanosheets. (b) TEM image of a unmodified single hexagonal nanosheet, with (c) the corresponding SAED pattern and (d) a high resolution TEM image showing the lattice fringes. (e) TEM image of a composite nanosheet, with (f-j) the corresponding EDS mapping. (f-Bi, g-Te, h-Co, i-Ni, j-Mo)

Figure 2 | XPS spectra of Bi_2Te_3 nanosheets modified with Co-Ni-Mo alloy modified NPs: (a) Bi 4f, (b) Te 3d, (c) Co 2p, (d) Ni 2p, (e) Mo 3d, and (f) O 1s.

Figure 3 | (a) AFM topograph of Bi_2Te_3 nanosheets. (b-c) SGM images of Bi_2Te_3 nanosheets. (d) Electrical signal recorded along the green line in (c)

Figure 4 | (a) LSV curves with different initial voltage of modified Bi_2Te_3 nanosheets on Ni foam in 0.9 M KOH solution, scan rate = 10 mV s^{-1}; inset shows CV curves of Ni foam and un-modified Bi_2Te_3 nanosheets on Ni foam in 0.9 M KOH solution. (b) LSV curves of different samples on Ni foam in 0.9 M KOH solution (Bi_2Te_3@CoNiMo means the Bi_2Te_3@$Co_{69.4}$NiMo-Ni foam).

Figure 5 | (a) LSV curves of samples on Ni foam in 0.9 M KOH solution, scan rate = 10 mV s^{-1}. (b) Onset potentials (E_{onset}) and potentials required to reach J = 10 mA cm^{-2} ($E_{J=10\ mA\ cm^{-2}}$) of the OER catalyzed by the prepared catalysts. (c) Tafel curves of samples on Ni foam in 0.9 M KOH solution. (d) TOF of samples on Ni foam in 0.9 M KOH solution (Bi_2Te_3@CoNiMo means the Bi_2Te_3@$Co_{69.4}$NiMo-Ni foam).

Figure 6 | (a) LSV of curves of Bi_2Te_3@CoNiMo samples with different Co concentrations on Ni foam in 0.9 M KOH solution, scan rate = 10 mV s^{-1}. (b) Tafel curves of samples on Ni foam in 0.9 M KOH solution. (c) EIS spectra of samples on Ni foam in 0.9 M KOH solution. (d) TOF curves of samples on Ni foam in 0.9 M KOH solution

Figure 7 | LSV of Bi_2Te_3@$Co_{69.4}$NiMo-Ni foam in 0.9 M KOH solution, scan rate = 10 mV s^{-1}; inset is a schematic illustration of the electrochemical reactions.

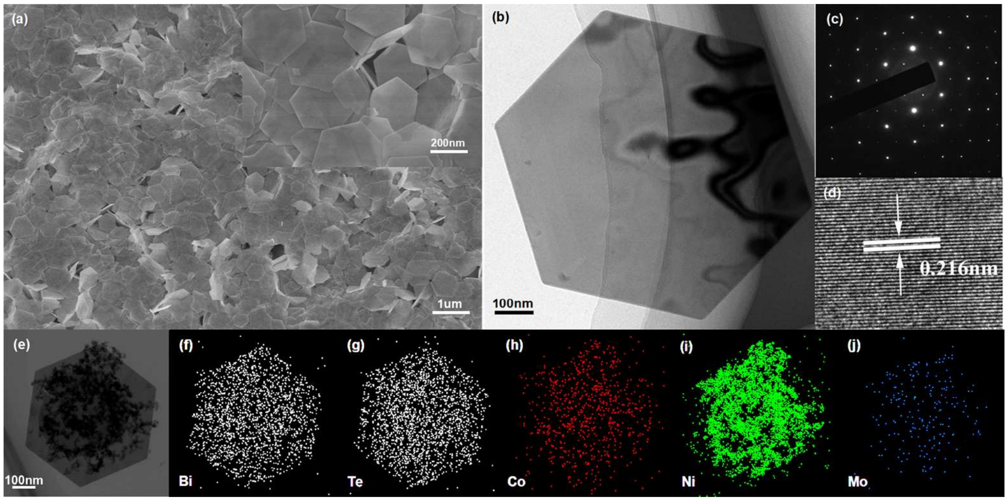

Figure 1 | (a) SEM image of unmodified Bi2Te3 nanosheets. (b) TEM image of a unmodified single hexagonal nanosheet, with (c) the corresponding SAED pattern and (d) a high resolution TEM image showing the lattice fringes. (e) TEM image of a composite nanosheet, with (f-j) the corresponding EDS mapping. (f-Bi, g-Te, h-Co, i-Ni, j-Mo)
515x254mm (120 x 120 DPI)

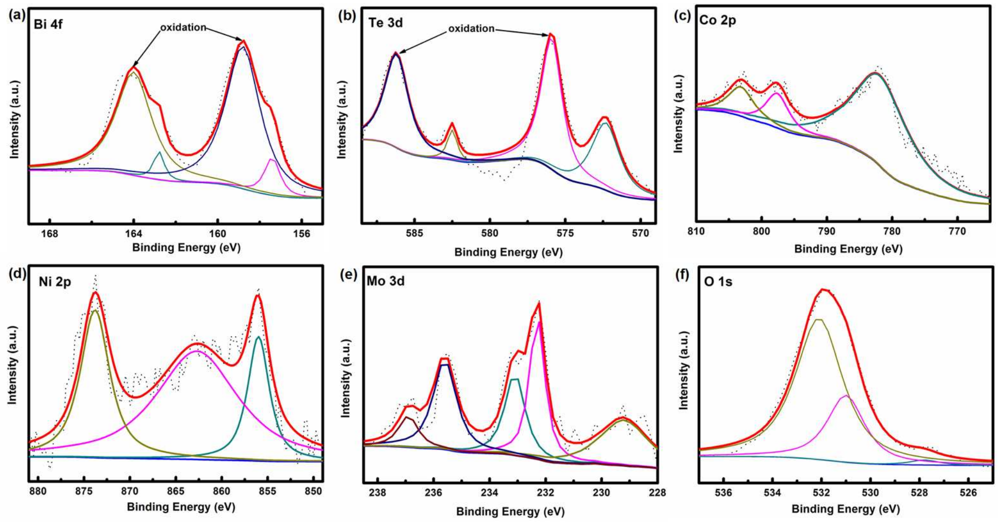

Figure 2 | XPS spectra of Bi2Te3 nanosheets modified with Co-Ni-Mo alloy modified NPs: (a) Bi 4f, (b) Te 3d, (c) Co 2p, (d) Ni 2p, (e) Mo 3d, and (f) O 1s.
589x306mm (96 x 96 DPI)

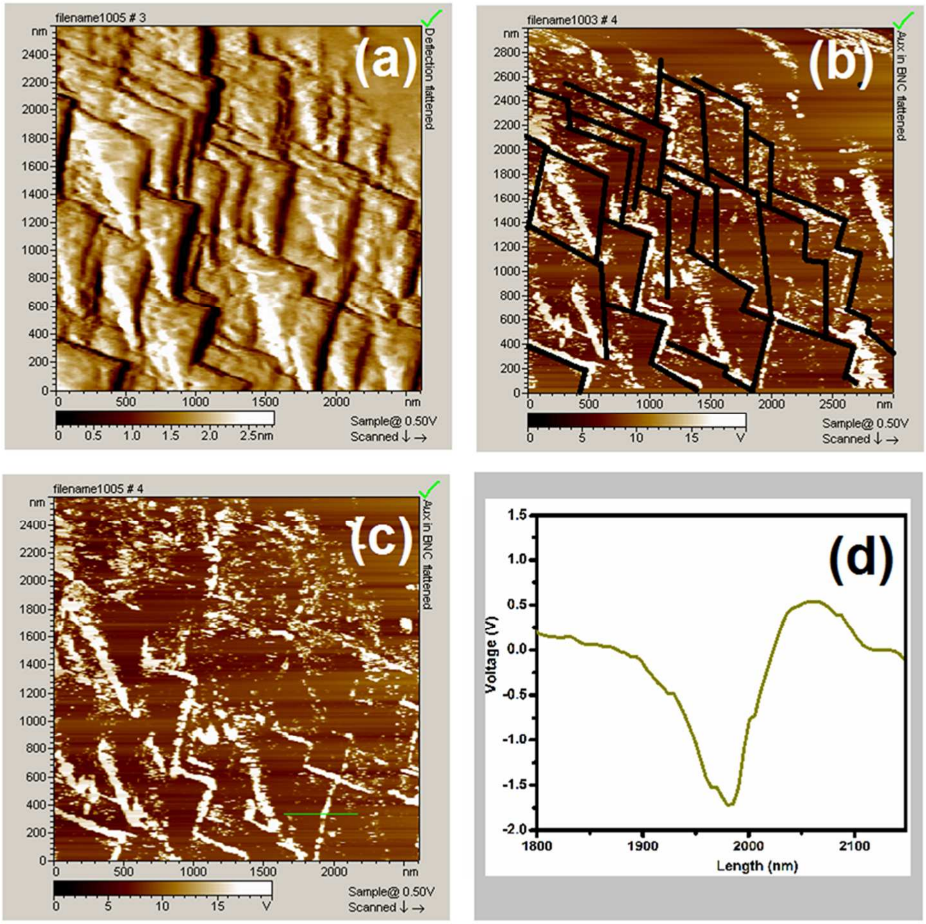

Figure 3 | (a) AFM topograph of Bi2Te3 nanosheets. (b-c) SGM images of Bi2Te3 nanosheets. (d) Electrical signal recorded along the green line in (c)
239x230mm (150 x 150 DPI)

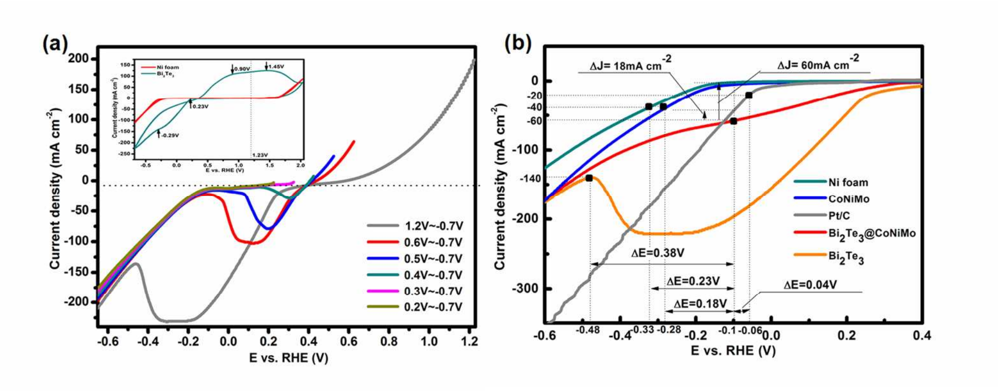

Figure 4 | (a) LSV curves with different initial voltage of modified Bi2Te3 nanosheets on Ni foam in 0.9 M KOH solution, scan rate = 10 mV s-1; inset shows CV curves of Ni foam and un-modified Bi2Te3 nanosheets on Ni foam in 0.9 M KOH solution. (b) LSV curves of different samples on Ni foam in 0.9 M KOH solution (Bi2Te3@CoNiMo means the Bi2Te3@Co69.4NiMo-Ni foam).
459x179mm (120 x 120 DPI)

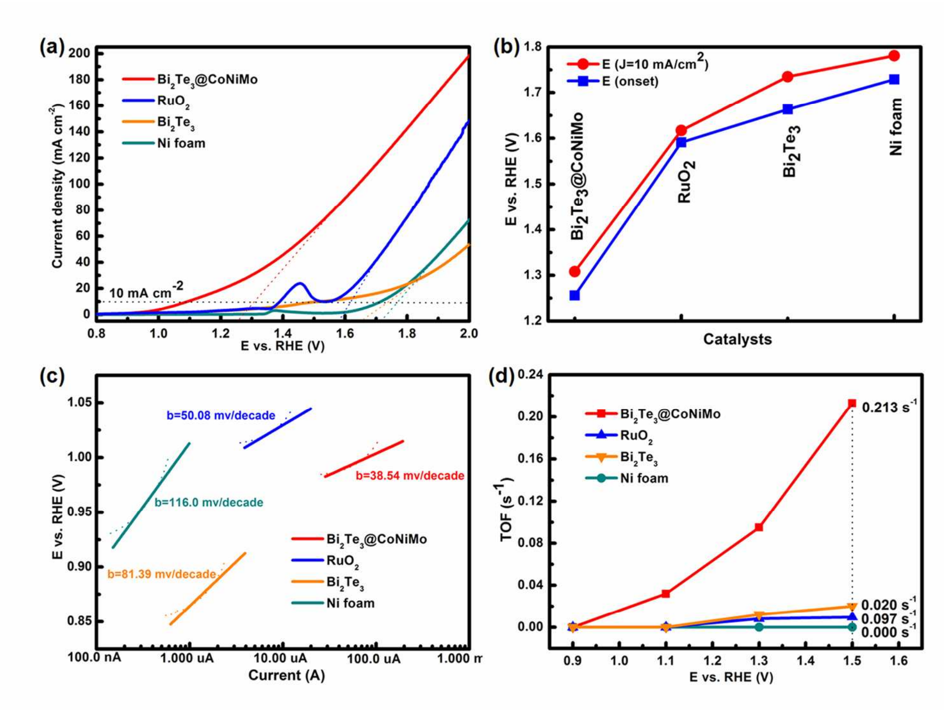

Figure 5 | (a) LSV curves of samples on Ni foam in 0.9 M KOH solution, scan rate = 10 mV s-1. (b) Onset potentials (Eonset) and potentials required to reach J = 10 mA cm-2 (EJ=10 mA cm-2) of the OER catalyzed by the prepared catalysts. (c) Tafel curves of samples on Ni foam in 0.9 M KOH solution. (d) TOF of samples on Ni foam in 0.9 M KOH solution (Bi2Te3@CoNiMo means the Bi2Te3@Co69.4NiMo-Ni foam).
464x329mm (96 x 96 DPI)

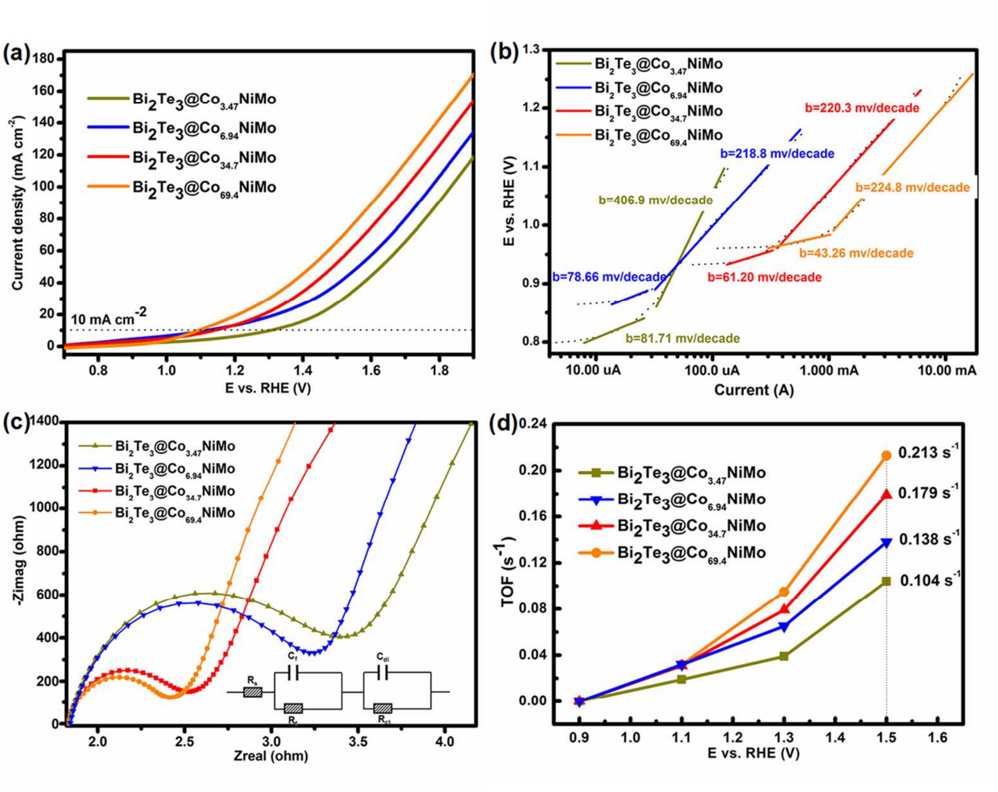

Figure 6 | (a) LSV of curves of Bi2Te3@CoNiMo samples with different Co concentrations on Ni foam in 0.9 M KOH solution, scan rate = 10 mV s-1. (b) Tafel curves of samples on Ni foam in 0.9 M KOH solution. (c) EIS spectra of samples on Ni foam in 0.9 M KOH solution. (d) TOF curves of samples on Ni foam in 0.9 M KOH solution

423x336mm (96 x 96 DPI)

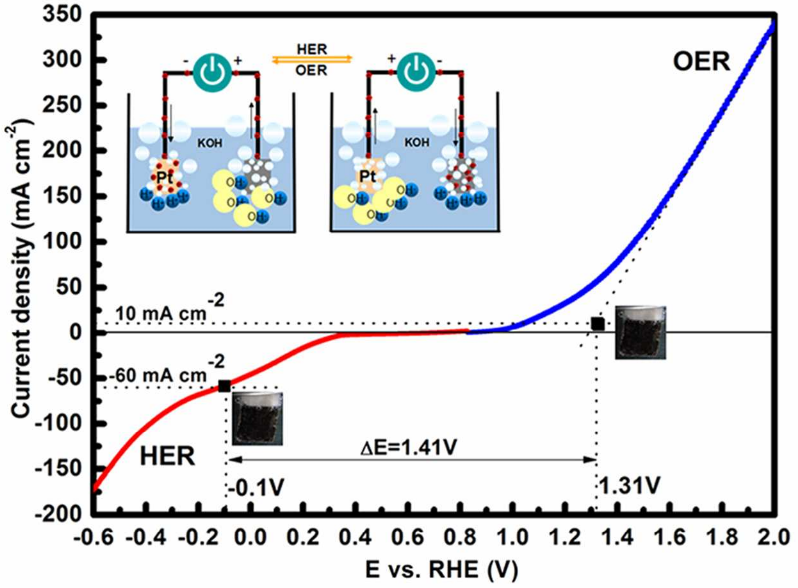

Figure 7 | LSV of Bi2Te3@Co69.4NiMo-Ni foam in 0.9 M KOH solution, scan rate = 10 mV s-1; inset is a schematic illustration of the electrochemical reactions.
254x177mm (120 x 120 DPI)

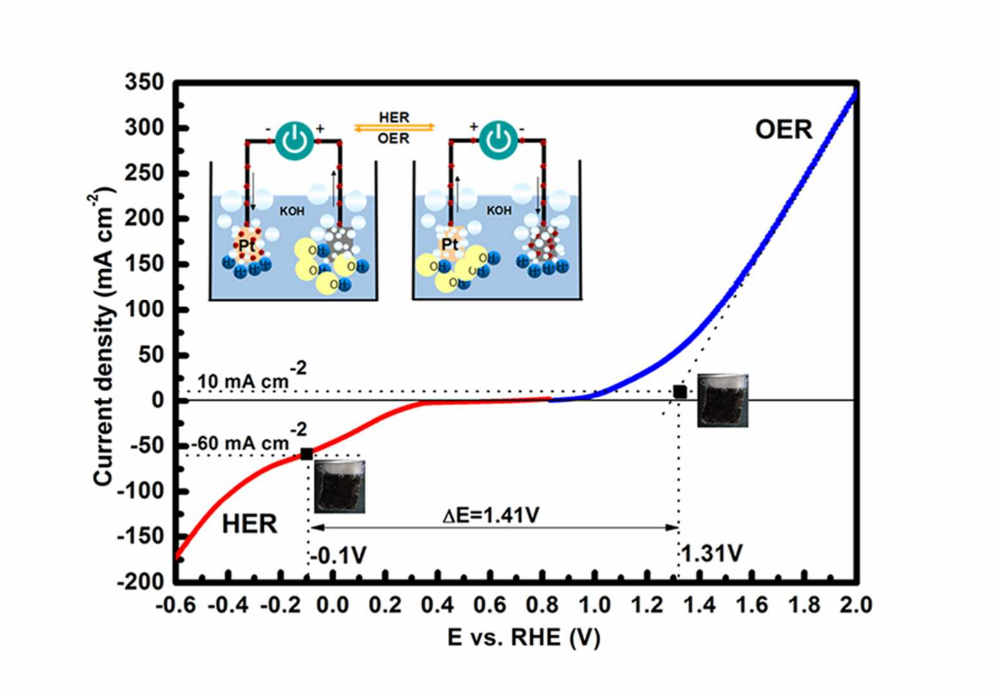

254x177mm (120 x 120 DPI)